Non-Migrating Tides in the Martian Atmosphere as Observed by MAVEN IUVS

Daniel Y. Lo,[1] Roger V. Yelle,[1] Nicholas M. Schneider,[2] Sonal K. Jain,[2] A. Ian F. Stewart,[2] Scott L. England,[3] Justin I. Deighan,[2] Arnaud Stiepen,[2] J. Scott Evans,[4] Michael H. Stevens,[5] Michael S. Chaffin,[2] Matteo M. J. Crismani,[2] William E. McClintock,[2] John T. Clarke,[6] Gregory M. Holsclaw,[2] Franck Lefèvre,[7] Bruce M. Jakosky[2]

Corresponding author: Daniel Y. Lo, Lunar and Planetary Laboratory, University of Arizona, Tucson, Arizona, USA (85721-0092). (danielloyw@gmail.com)

[1]Lunar and Planetary Laboratory,

This article has been accepted for publication and undergone full peer review but has not been through the copyediting, typesetting, pagination and proofreading process which may lead to differences between this version and the Version of Record. Please cite this article as doi: 10.1002/2015GL066268

Using the Mars Atmospheric and Volatile EvolutioN Mission (MAVEN) Imaging Ultraviolet Spectrograph (IUVS), we found periodic longitudinal variations in CO_2 density in the Martian atmosphere. These density variations are derived from observations of the CO_2^+ ($B^2\Sigma^+ \rightarrow X^2\Pi$) emission from

University of Arizona, Tucson, Arizona, USA.

[2]Laboratory for Atmospheric and Space Physics, University of Colorado Boulder, Boulder, Colorado, USA.

[3]Space Sciences Laboratory, University of California Berkeley, Berkeley, California, USA.

[4]Computational Physics, Inc., Springfield, Virginia, USA.

[5]Naval Research Laboratory, Washington D. C., USA.

[6]Center for Space Physics, Boston University, Boston, Massachusetts, USA.

[7]Laboratoire ATmosphères, Milieux, Observations Spatiales, Centre National de la Recherche Scientifique, Paris, France.

limb scans in the $100 - 190$ km altitude range. The variations exhibit significant structure with longitudinal wavenumbers 1, 2 and 3 in an effectively constant local solar time frame, and we attribute this structure to non-migrating tides. The wave-2 component is dominated by the diurnal eastward-moving DE1 tide at the equator and the semidiurnal stationary S0 tide at the midlatitudes. Wave-3 is dominated by the diurnal eastward-moving DE2 tide, with possibly the semidiurnal eastward-moving SE1 tide causing an amplitude increase at the midlatitudes. Structure in the wave-1 component can be explained by the semidiurnal westward-moving SW1 tide.

1. Introduction

Diurnal solar forcing of planetary atmospheres can produce tides, global-scale oscillations in density, pressure and temperature with periods which are harmonics of the solar day. Tides have been observed throughout the atmosphere, from the equatorial region [*Withers et al.*, 2003] to the high northern and southern latitudes [*Cahoy et al.*, 2007; *Withers et al.*, 2011], and from the surface [*Wilson and Hamilton*, 1996] to 160 km altitude [*Withers et al.*, 2003]. Numerical simulations (e.g. *Forbes et al.* [2002]) predict that these tides can extend further up to 200 km.

Because of the widespread occurrence of tides, and also because tides can produce significant deviations in atmospheric state variables from their equilibrium values, a comprehensive study is critical for understanding the variability of the atmosphere and the circulation and transport processes that stem from this variability. Regions of turbulence can form from instabilities within the tidal fields, lifting suspended dust, water vapor and other atmospheric constituents into the upper atmosphere [*Zurek*, 1976]. By controlling the densities of various atmospheric constituents directly or indirectly through such induced transport processes, tides can strongly influence atmospheric chemistry, ultimately exerting an indirect control on atmospheric loss rates. These far-reaching effects of tides imply that no understanding of the atmosphere can be complete without an understanding of atmospheric tides.

Using CO_2^+ UV doublet ($B^2\Sigma^+ \rightarrow X^2\Pi$) emission profiles obtained from limb scans with the Imaging Ultraviolet Spectrograph (IUVS) [*McClintock et al.*, 2014] on board the Mars Atmospheric and Volatile EvolutioN Mission (MAVEN) spacecraft [*Jakosky et al.*, 2015], we investigate the variation of CO_2 density with latitude and longitude in a fixed local solar time (LST) frame. We observe significant spatial structure in the density variations and attribute this structure to tides.

In the next section, we provide some background information for understanding atmospheric tides and the CO_2^+ UV doublet emission. Section 3 describes the observations, while Section 4 explains the steps in the processing to obtain the CO_2 density. Results appear in Section 5, with some discussion on the interpretation of the observed wave structures. We conclude in Section 6.

2. Background

2.1. Atmospheric Tides

Tides describe the intrinsic oscillatory modes of the planetary atmosphere in response to the diurnal solar forcing. The latitudinal and longitudinal structure of each tide is separable from the vertical structure [*Chapman and Lindzen*, 1970; *Forbes*, 1995]. Altitudinal dependence is described by a characteristic vertical wavelength, and evanescent modes with small vertical wavelengths decay rapidly with altitude. Latitudinal variations are described by Hough functions. Longitudinal variations are represented mathematically as a series of cosines [*Forbes et al.*, 2002]:

$$\sum_s \sum_n A_{s,n} \cos[(s-n)\lambda + n\Omega t + \delta_{s,n}] \tag{1}$$

where s is the zonal wavenumber, Ω is the planetary rotation rate, λ is the east longitude, t is the local solar time (LST). Tides with $n = 1, 2$ are diurnal and semidiurnal respectively. $A_{s,n}$ and $\delta_{s,n}$ are the amplitude and phase of the individual tides, identified by the (s, n)

label [*Chapman and Lindzen*, 1970; *Forbes*, 1995]. Solar forcing on a zonally symmetric planet gives rise to migrating or sun-synchronous tides, characterized by $s = n$. Zonal asymmetries, such as in topography, surface thermal inertia, surface albedo and dust, can interact with the solar forcing to produce non-migrating tides, with $s \neq n$ [*Forbes*, 2004].

When observed in a fixed LST reference frame, longitudinal variations due to the (s, n) tide will manifest as a wave-$|s - n|$ structure, offset by an apparent phase $\delta'_{s,n}$ that has a magnitude equal to $n\Omega t + \delta_{s,n}$:

$$A_{s,n} \cos[|s - n|\lambda + \delta'_{s,n}] \tag{2}$$

In such a reference frame, an observer will not be able to observe variations due to migrating tides (Equation 2 reduces to a constant over all longitudes with $s = n$). However, this same observer will be able to observe longitudinal variations from non-migrating tides, with each wave-k structure being the sum of non-migrating tides with $|s - n| = k$. Identification of the dominant tides behind that structure involves the comparison of the observed amplitudes and phases, and their dependence on latitude and altitude to model results of specific tidal modes. Such is the case for this study, and we shall henceforth discuss only non-migrating tides.

Previous observations and simulations of the Martian atmosphere have found several dominant non-migrating tides. The diurnal eastward $(-1, 1)$ tide, also referred to as DE1, has been inferred from wave-2 structure in surface pressure data from Viking [*Wilson and Hamilton*, 1996], temperature measurements in the lower atmosphere by Thermal Emission Spectrometer (TES) [*Banfield et al.*, 2003; *Wilson*, 2000] and the middle atmosphere by Mars Climate Sounder (MCS) [*Guzewich et al.*, 2012], upper atmosphere densities from aerobraking [*Wilson*, 2002; *Withers et al.*, 2003] and atmospheric profiles inferred from observations by SPectroscopy for Investigation of Characteristics of the Atmosphere of Mars (SPICAM) [*Withers et al.*, 2011]. Amplitudes are found to be $\sim$ 20% of the equilibrium value in the upper atmosphere over the tropics and the midlatitudes, decreasing towards the poles [*Withers et al.*, 2003, 2011]. This is consistent with numerical simulations [*Bougher et al.*, 2004; *Angelats i Coll et al.*, 2004; *Wilson*, 2002; *Forbes and Miyahara*, 2006], which returned amplitudes of $10\% - 40\%$.

Wave-3 structure is typically smaller than the wave-2 component, and has been attributed to two tides. The DE2 $(-2, 1)$ tide has been observed in TES temperature data by *Wilson* [2000] and *Banfield et al.* [2003], and in MCS data by *Guzewich et al.* [2012] and *Moudden and Forbes* [2014]. Observations of atmospheric densities [*Withers et al.*, 2003] and electron densities [*Bougher et al.*, 2001, 2004; *Cahoy et al.*, 2007] at high latitudes found the semidiurnal SE1 $(-1, 2)$ tide to dominate instead. To reconcile the seemingly contradictory conclusions from the various studies, *Wilson* [2002] and *Withers et al.* [2011] suggested that DE2 is dominant at the equatorial region, while SE1 is dominant at the high latitudes. This hypothesis is later confirmed by *Wolkenberg and Wilson* [2014].

The wave-1 component is typically weaker than both wave-2 and wave-3. Due to the large observational uncertainties associated with lower signal strength, it has been difficult attributing this component to particular tides [*Withers et al.*, 2003, 2011]. Modeling by *Moudden and Forbes* [2008] suggests that the diurnal stationary D0 $(0, 1)$ tide and the semidiurnal westward SW1 $(1, 2)$ tide may be significant.

2.2. CO_2^+ UV Doublet Emission

Often referred to as the UV doublet (UVD), the CO_2^+ ($B^2\Sigma^+ \rightarrow X^2\Pi$) electronic transition system at 289 nm provides a direct measure of CO_2 densities in the Martian atmosphere. $CO_2^+(B^2\Sigma^+)$ is generated from CO_2 via photoionization and photoelectron impact, and from $CO_2^+(X^2\Pi)$ by solar photons via fluorescent scattering [*Fox*, 2004]. Studies by *Fox and Dalgarno* [1979], *Jain and Bhardwaj* [2012] and *Stiepen et al.* [2015] have found photoionization and photoelectron impact to be the dominant mechanisms, with fluorescent scattering accounting for 1% of total UVD emission rates at $\sim$ 130 km and $<$ 25% at $\sim$ 180 km. This dominance of photoionization and photoelectron impact means that CO_2^+ UVD volume emission rates are effectively controlled by CO_2 density and the solar EUV flux. Since the solar EUV flux is uniform over the sunlit planetary disk, spatial variations in UVD intensity can be used to infer variations in the CO_2 density.

3. Observations

Data used in this study come from limb scans performed by the Imaging Ultraviolet Spectrograph (IUVS) on the MAVEN spacecraft. Details of IUVS operation and observational phases can be found in *McClintock et al.* [2014]. Briefly, IUVS is mounted on an Articulated Payload Platform (APP) which allows for controlled orientation of the instrument slit as it captures spectra of the planet in the FUV ($110 - 190$ nm) and MUV ($180 - 340$ nm) channels. Limb scans are taken near the periapses, with the slit pointed perpendicularly and to the right of the direction of motion [*Jain et al.*, 2015]. A scan mirror sweeps the slit up and down, allowing IUVS to map the vertical profile of the atmosphere with an altitude resolution of $\sim$ 7 km. 12 scans are taken in this manner with each periapse pass. With the slit spanned by 7 spatial bins, a total of 84 limb profiles are taken during the periapse observational phase of each orbit.

This study makes use of periapse limb profiles obtained with the MUV channel from Orbit 109 (start time 18 October 2014 16:05 UT) to Orbit 128 (start time 22 October 07:49 UT), corresponding to a solar longitude $L_s = 217° - 219°$. No data was taken during Orbit 115, as the spacecraft stood down due to dust concerns associated with the passage of Comet Siding Spring [*Schneider et al.*, 2015]. In order to constrain our observations to a narrow range in LST for the observation of non-migrating tides, only profiles from scans $6 - 12$ are used in this study. For this set of profiles, all observations are taken between $1340 - 1500$ LST. With each periapse pass, the tangent latitude of the line of sight migrates southward from $\sim 44°$ to $\sim -5°$ while the tangent longitude varies by $\sim 15°$. Spacecraft altitude increases from ~ 190 km at scan 6 to ~ 530 km at scan 12. Between successive orbits, longitudinal coverage changes by $\sim 67°$ eastward, with every 16th orbit returning to approximately the same longitude. A total of 873 profiles is used in our analysis.

4. Analysis

Raw data are processed through the standard pipeline for IUVS periapse limb scans. After removing the detector dark current, the digital numbers are converted into physical intensities using a calibration curve based on observations of UV-bright stars, with an appropriate scaling by instrument geometric factors for extended source observations. CO_2^+ UVD emissions are then isolated from the calibrated spectra using a Multiple Linear Regression (MLR) algorithm. The MLR algorithm involves the scaling and fitting of reference spectra for all known emissions in the MUV region [*Stevens et al.*, 2015]. In the 289 nm region, the only significant spectral features are the UVD band and a background signal that follows the spectral shape of the Sun. This latter component is still being investigated but is likely due to scatter by aerosols in the Martian atmosphere, possibly with an additional contribution from instrumental stray light. In either case the spectral shape of the UVD and the solar component differ greatly and separation is straightforward.

We adopt an empirical approach to determine the CO_2 density from the measured intensity. The volume emission rate is parameterized as a Chapman profile and the measured intensity is fitted to the integral of the volume emission rate along the line of sight:

$$I = 2\int_b^\infty C\sigma n_0 \exp\left(\frac{z_0 - z}{H} - \frac{\sigma n_0 H}{\mu_0} e^{(z_0-z)/H}\right) \frac{r dz}{\sqrt{r^2 - b^2}}$$

where z is the altitude, b is the impact parameter measured from the center of the planet, $r = R + z$ with R being the planetary radius, σ is the absorption cross-section for the UV photon, n_0 is the number density of CO_2 at the reference altitude z_0, H is the atmospheric scale height, μ_0 is the cosine of the solar zenith angle, and C is a proportionality factor that accounts for the solar flux and any calibration factors. z_0 is set to be 130 km for ease of comparison with other studies of Martian atmospheric tides. Three parameters are allowed to vary in the fitting process: C, H, and σn_0, which we refer to as the scaled density. Because the fit is done over an altitude range of $100 - 190$ km, it will be more sensitive to tides with long vertical wavelengths that span a larger fraction of that window. Figure 1 shows some fits to the MLR-derived profiles.

Of course, we do not expect the volume emission rate to rigorously follow a Chapman profile. The Chapman layer is used here as a convenient way to empirically characterize the emissions rather than a rigorous description of the excitation process. Nonetheless, because the Chapman layer is an approximation to the UVD emission processes, its emission profile possesses the correct shape and, as shown in Figure 1, the fits based on this approach are excellent. The analytic form of this Chapman approximation allows us to easily determine the value of $\sigma n_\circ$ for characterizing CO_2 density variations in the atmosphere. As the fits in Figure 1 show, the scaled density controls the altitude of the emission peak, essentially the altitude of the maximum CO_2 photoionization rate. The Chapman profile does rigorously describe the variation of emission rate with solar zenith angle to the extent that the atmosphere can be treated as plane-parallel. Thus it satisfies our objective in providing a good measure of the relative CO_2 density variations in the atmosphere. In addition, the derived scaled densities will not be sensitive to the detector calibration. Although there are uncorrected flatfield effects that result in sensitivity variations of $\sim 10\%$ across the spatial bins, these will only change the value of C rather than the scaled density.

5. Results and Discussion

Figure 2 shows an overview of variations in CO_2 density with latitude and longitude. Because IUVS coverage returns to a similar longitude every 16th orbit, we are able to determine these variations to be persistent in a fixed LST frame, leading to our interpretation of the observed structures as tides. Along the equator, we observe a strong wave-2 tidal component, with peaks occurring at 75°E and 225°E. The amplitude of this component decreases towards higher latitude. There is also a smaller set of peaks at $\sim 40°$N, at a different apparent phase from the equatorial component.

As discussed previously, identification of the dominant tides requires the decomposition of the structure into components of different wavenumbers, and subsequent analysis of the amplitudes and phases. Grouping profiles into 10° latitude bands, we fit sinusoids of wavenumber 1, 2 and 3 to the scaled density values. Figure 3 shows the fits between $-5°$N and 5°N and between 35°N and 45°N. Figure 4 shows the amplitudes A' normalized to the equilibrium values and apparent phases δ' from the fits, with Table 1 showing the plotted values.

As anticipated from Figure 2, the wave-2 component has the largest average amplitude, with a peak of 29% at $\sim 10°$N, decreasing to 6% at $\sim 30°$N. This structure is characteristic of the DE1 tide which has been identified as the dominant mode at the equatorial region by the previous studies detailed in Section 2.1. Further confirmation of a dominant DE1 tide comes from the phase, which has been found to change minimally with season from the surface to 130 km [*Wilson*, 2002]. After correcting for the LST, we find a phase of $253 \pm 7°$ at the equator, comparable to the phase of $286 \pm 20°$ (averaged over $-5°$N and 5°N) observed by *Withers et al.* [2003]. Northwards of $\sim 30°$N, the amplitude increases slightly to 8%, with a significant decrease in apparent phase. This change in apparent phase, together with the amplitude trending in the opposite direction expected from the DE1 tide, suggest another tide becoming dominant at the higher latitudes. Modeling by *Moudden and Forbes* [2008] found the semidiurnal stationary S0 $(0, 2)$ tide increasing to 20% of the DE1 peak amplitude at $\sim 40°$N, consistent with our observations. If we assume that these model results remain valid over different seasons ($L_s = 26° - 92°$ for *Moudden and Forbes* [2008]), then the amplitude increase in the wave-2 component at the higher latitudes can be explained by the S0 tide.

The average amplitude of the wave-3 component is slightly smaller than that for wave-2, decreasing from 18% from the equator with latitude. This latitudinal structure agrees well with previous studies such as *Bougher et al.* [2001], *Bougher et al.* [2004], *Withers et al.* [2003] and *Withers et al.* [2011], and points to the DE2 tide, rather than SE1 which instead has a local maximum at $\sim 20°$N. This is consistent with the observations by *Wilson* [2002] and *Withers et al.* [2011] that DE2 dominates at equatorial latitudes. Phases show only a rough correspondence however, with values of $25 \pm 7°$, $54 \pm 9°$ and $\sim 90°$ for this study, *Withers et al.* [2003] and *Wilson* [2002] respectively. This discrepancy in phase may be due to the different seasons at which the observations for the various studies were conducted. At $30° - 40°$N, a reversal in the amplitude trend expected from DE2 together with a large change in apparent phase of 200° (almost a flip in the tidal structure) point to the presence of another dominant tide at the higher latitudes. The amplitude increase is consistent with SE1 becoming dominant at the higher latitudes, but a poor correspondence in phases and the constraint of observations to a single LST in this study prevent a conclusive identification.

While previous observational studies have detected a weak but significant wave-1 component, these studies were unable to pinpoint the dominant tides producing this wave-1 signal. Our fitted wave-1 component exhibits a sharp peak at $\sim 20°$N, which resembles the structure for the SW1 (1, 2) tide as modeled by *Moudden and Forbes* [2008]. Beneath the peak, the observed amplitude also shows a general decrease towards the north, another feature consistent with the modeled SW1 tide. With the same caveat regarding potentially unknown seasonal dependences, we suggest that the wave-1 structure is dominated by the SW1 tide.

6. Conclusions

Examining variations in CO_2 scaled densities derived from fitting Chapman profiles to CO_2^+ UVD emissions from IUVS limb scans, we are able to observe significant wave-1, wave-2 and wave-3 tidal structure at $100 - 190$ km altitude. Amplitudes of all three components are consistent with previous observations and modeling results. Wave-2 is dominated by DE1 at the equator, with S0 being a possible explanation for the structure observed at the midlatitudes. Wave-3 structure is consistent with DE2 and SE1 at the equator and midlatitudes respectively, but this cannot be confirmed by a phase comparison. Wave-1 appears to be dominated by SW1.

Generally, identification of tides in this study is complicated by an uncertainty that stems from a poor understanding of how tides in the upper Martian atmosphere change with the seasons. This uncertainty should not persist for long however. The dataset used in this study is but a small fraction of all limb scan data that will come from MAVEN IUVS. This study demonstrates that even with a limited dataset we are able to draw significant conclusions, and is a prelude to the science that can come from an expanding dataset as MAVEN proceeds through its mission. We will be able to investigate seasonal changes in the tidal structures, and also better characterize the vertical structure of tides with the larger volume of data. The precession of the spacecraft orbit will allow us to sample densities at a different LST, to better characterize phases of the various tides, and to go beyond the restrictions of the constant LST frame and start observing migrating tides. These additional dimensions to the data will be able to provide more constraints for the validation of atmospheric models, ultimately forming the foundation for the comprehensive study we need to understand the behavior and effects of thermal tides in the Martian atmosphere.

Acknowledgments. The data used in the study are archived in the Planetary Atmospheres Node of the Planetary Data System at http://atmos.nmsu.edu/data_and_services/atmospheres_data Each filename is marked with the identifier "periapse", the orbit number, the start time of the observation, and "v02_r01" reflecting the version of the calibration curve and MLR decomposition. The MAVEN project is supported by NASA through the Mars Exploration Program. Arnaud Stiepen is supported by the Belgian American Educational Foundation and the Rotary District 1630. The authors thank Steve Bougher, John Wilson and Paul Withers for providing critical and valuable comments towards the improvement of this manuscript in their reviews.

References

Angelats i Coll, M., F. Forget, M. A. Lopez-Valverde, P. L. Read, and S. R. Lewis (2004), Upper atmosphere of Mars up to 120 km: Mars Global Surveyor accelerometer data analysis with the LMD general circulation model, *Journal of Geophysical Research*, *109*, E01011, doi:10.1029/2003JE002163.

Banfield, D., B. J. Conrath, M. D. Smith, P. R. Christensen, and R. J. Wilson (2003), Forced waves in the Martian atmosphere from MGS TES nadir data, *Icarus*, *161*, 319–345, doi:10.1016/j.icarus.2004.03.015.

Bougher, S. W., S. Engel, D. P. Hinson, and J. M. Forbes (2001), Mars Global Surveyor Radio Science electron density profiles: Neutral atmosphere implications, *Geophysical Research Letters*, *28*(16), 3091–3094.

Bougher, S. W., S. Engel, D. P. Hinson, and J. R. Murphy (2004), MGS Radio Science electron density profiles: Interannual variability and implications for the Martian neutral atmosphere, *Journal of Geophysical Research*, *109*, E03010, doi:10.1029/2003JE002154.

Cahoy, K. L., D. P. Hinson, and G. L. Tyler (2007), Characterization of a semidiurnal eastward-propagating tide at high northern latitudes with Mars Global Surveyor electron density profiles, *Geophysical Research Letters*, *34*, L15201, doi:10.1029/2007GL030449.

Chapman, S., and R. Lindzen (1970), *Atmospheric tides. Thermal and gravitational*, D. Reidel, Dordrecht, Netherlands.

Forbes, J. M. (1995), *Tidal and planetary waves*, 67–87 pp., American Geophysical Union, Washington, D. C., doi:10.1029/GM087p0067.

Forbes, J. M. (2004), Tides in the middle and upper atmospheres of Mars and Venus, *Advances in Space Research*, *33*(2), 125–131, doi:10.1016/j.asr.2003.05.007.

Forbes, J. M., and S. Miyahara (2006), Solar semidiurnal tide in the dusty atmosphere of Mars, *Journal of the Atmospheric Sciences*, *63*(7), 1798–1817, doi:10.1175/JAS3718.1.

Forbes, J. M., F. C. Bridger, Alison, S. W. Bougher, M. E. Hagan, J. L. Hollingsworth, G. M. Keating, and J. Murphy (2002), Nonmigrating tides in the thermosphere of Mars, *Journal of Geophysical Research*, *107*(E11), 5113, doi:10.1029/2001JE001582.

Forget, F., F. Montmessin, J.-L. Bertaux, F. González-Galindo, S. Lebonnois, E. Quémerais, A. Reberac, E. Dimarellis, and M. A. López-Valverde (2009), Density and temperatures of the upper Martian atmosphere measured by stellar occultations with Mars Express SPICAM, *Journal of Geophysical Research: Planets*, *114*, E01,004, doi:10.1029/2008JE003086.

Fox, J. L. (2004), CO_2^+ dissociative recombination: A source of thermal and nonthermal C on Mars, *Journal of Geophysical Research*, *109*, A08,306, doi:10.1029/2004JA010514.

Fox, J. L., and A. Dalgarno (1979), Ionization, luminosity, and heating of the upper atmosphere of Mars, *Journal of Geophysical Research*, *86*(A12), 7315–7333, doi:10.1029/JA086iA02p00629.

Guzewich, S. D., and E. R. Talaat, and D. W Waugh (2012), Observations of planetary waves and nonmigrating tides by the Mars Climate Sounder, *Journal of Geophysical Research: Planets*, *117*, E03010, doi:10.1029/2011JE003924.

Jakosky, B. M., R. P. Lin, J. M. Grebowsky, J. G. Luhmann, D. F. Mitchell, G. Beutelschies, T. Priser, M. Acuna, L. Andersson, D. Baird, D. Baker, R. Bartlett, M. Benna, S. Bougher, D. Brain, D. Carson, S. Cauffman, P. Chamberlin, J.-Y. Chaufray, O. Cheatom, J. Clarke, J. Connerney, T. Cravens, D. Curtis, G. Delory, S. Demcak, A. DeWolfe, F. Eparvier, R. Ergun, A. Eriksson, J. Espley, X. Fang, D. Folta, J. Fox, C. Gomez-Rosa, S. Habenicht, J. Halekas, G. Holsclaw, M. Houghton, R. Howard,

M. Jarosz, N. Jedrich, M. Johnson, W. Kasprzak, M. Kelley, T. King, M. Lankton, D. Larson, F. Leblanc, F. Lefevre, R. Lillis, P. Mahaffy, C. Mazelle, W. McClintock, J. McFadden, D. L. Mitchell, F. Montmessin, J. Morrissey, W. Peterson, W. Possel, J.-A. Sauvaud, N. Schneider, W. Sidney, S. Sparacino, A. I. F. Stewart, R. Tolson, D. Toublanc, C. Waters, T. Woods, R. Yelle, R. Zurek (2015), The Mars Atmosphere and Volatile Evolution (MAVEN) Mission, *Space Science Reviews*, doi:10.1007/s11214-015-0139-x.

Jain, S. K., and A. Bhardwaj (2011), Model calculation of N_2 Vegard-Kaplan band emissions in Martian dayglow, *Journal of Geophysical Research: Planets*, *116*, E07005, doi:10.1029/2010JE003778.

Jain, S. K., and A. Bhardwaj (2012), Impact of solar EUV flux on CO Cameron band and CO_2^+ UV doublet emissions in the dayglow of Mars, *Planetary and Space Science*, *63-64*, 110–122, doi:10.1016/j.pss.2011.08.010.

Jain, S. K., A. I. F. Stewart, N. M. Schneider, J. I. Deighan, A. Stiepen, J. S. Evans, M. H. Stevens, M. S. Chaffin, W. E. McClintock, J. T. Clarke, G. M. Holsclaw, B. M. Jakosky (2015), The structure and variability of Mars upper atmosphere as seen in MAVEN/IUVS dayglow observations, *Geophysical Research Letters*, *42*, doi:10.1002/2015GL065419.

Lee, C., W. G. Lawson, M. I. Richardson, N. G. Heavens, A. Kleinbohl, D. Banfield, D. J. McCleese, R. W. Zurek, D. Kass, J. T. Schofield, C. B. Leovy, F. W. Taylor, and A. D. Toigo. (2009), Thermal tides in the Martian middle atmosphere as seen by the Mars Climate Sounder, *Journal of Geophysical Research: Planets*, *114*, E03005, doi:10.1029/2008JE003285.

McClintock, W. E., N. M. Schneider, G. M. Holsclaw, J. T. Clarke, A. C. Hoskins, A. I. Stewart, F. Montmessin, R. V. Yelle, and J. Deighan (2014), The Imaging Ultraviolet Spectrograph (IUVS) for the MAVEN Mission, *Space Science Reviews*, doi: 10.1007/s11214-014-0098-7.

Moudden, Y., and J. M. Forbes (2008), Topographic connections with density waves in Mars' aerobraking regime, *Journal of Geophysical Research: Planets*, *113*, E11009, doi: 10.1029/2008JE003107.

Moudden, Y., and J. M. Forbes (2014), Insight into the seasonal asymmetry of nonmigrating tides on Mars, *Geophysical Research Letters*, *41*, 2631–2636, doi: 10.1029/2008JE003107.

Schunk, R., and A. Nagy (2009), *Ionospheres: Physics, plasma physics, and chemistry*, Cambridge University Press, Cambridge, UK.

Schneider, N. M., J. I. Deighan, A. I. F. Stewart, W. E. McClintock, S. K. Jain, M. S. Chaffin, A. Stiepen, M. Crismani, J. M. C. Plane, J. D. Carrillo-Sanchez, J. S. Evans, M. H. Stevens, R. V. Yelle, J. T. Clarke, G. M. Holsclaw, F. Montmessin, B. M. Jakosky (2015), MAVEN IUVS observations of the aftermath of the Comet Siding Spring meteor shower on Mars, *Geophysical Research Letters*, *42*, doi:10.1002/2015GL063863.

Stevens, M. H., J. S. Evans, N. M. Schneider, A. I. F. Stewart, J. Deighan, S. K. Jain, W. E. McClintock, G. M. Holsclaw, J. T. Clarke and B. M. Jakosky (2015), New observations of molecular nitrogen in the Martian upper atmosphere by IUVS on MAVEN, *Geophysical Research Letters*, *42*, doi:10.1002/2015GL065319.

Stiepen, A., Gerard, J.-C., Bougher, S. W., Montmessin, F., Hubert, B., Bertaux, J.-L. (2015), Mars thermospheric scale height: CO Cameron and CO_2^+ dayglow observations from Mars Express, *Icarus*, *245*, 295–305, doi:10.1016/j.icarus.2014.09.051.

Wilson, R. J. (2002), Evidence for diurnal period Kelvin waves in the Martian Atmosphere from Mars Global Surveyor TES data, *Geophysical Research Letters*, *27*(23), 3889–3892, doi:10.1029/2000GL012028.

Wilson, R. J. (2002), Evidence for nonmigrating thermal tides in the Mars upper atmosphere from the Mars Global Surveyor Accelerometer Experiment, *Geophysical Research Letters*, *29*(7), 1120–1123, doi:10.1029/2001GL013975.

Wilson, R. J., and K. Hamilton (1996), Comprehensive model simulation of thermal tides in the Martian atmosphere, *Journal of the Atmospheric Sciences*, *53*(9), 1290–1326, doi:10.1175/1520-0469(1996)053<1290:CMSOTT>2.0.CO;2.

Withers, P., S. W. Bougher, and G. M. Keating (2003), The effects of topographically-controlled thermal tides in the martian upper atmosphere as seen by the MGS accelerometer, *Icarus*, *164*, 14–32, doi:10.1016/S0019-1035(03)00135-0.

Withers, P., R. Pratt, J.-L. Bertaux, and F. Montmessin (2011), Observations of thermal tides in the middle atmosphere of Mars by the SPICAM instrument, *Journal of Geophysical Research: Planets*, *116*, E11,005, doi:10.1029/2011JE003847.

Wolkenberg, P., and R. J. Wilson (2014), Mars Climate Sounder observations of wave structure in the north polar middle atmosphere of Mars during the summer season, *Eighth International Conference on Mars, Pasadena, CA*, Abstract 1219.

Zurek, R. W. (1976), Diurnal tide in the Martian atmosphere, *Journal of the Atmospheric Sciences*, *33*(2), 321–337, doi:10.1175/1520-0469(1976)033<0321:DTITMA>2.0.CO;2.

Zurek, R. W. (1988), Free and forced modes in the Martian atmosphere, *Journal of Geophysical Research*, *93*(D8), 9452–9462, doi:10.1029/JD093iD08p09452.

sampleProfile.pdf

Figure 1. Chapman layer fits to isolated CO_2^+ UVD profiles at $\sim 10°$N and different longitudes. All profiles are from scan 10 spatial bin 4 of the respective orbits. Error bars denote 1σ random uncertainties in the measurements. The higher density at 221°E gives rise to a higher altitude of the emission peak (indicated by the arrows).

Table 1. Fitted amplitudes A'_k normalized to zonal mean and apparent phases δ'_k for various latitude bands for wavenumbers $k = 1, 2, 3$.

Latitude	A'_1	δ'_1	A'_2	δ'_2	A'_3	δ'_3
−5°N to 5°N	$13\% \pm 2\%$	$263° \pm 10°$	$20\% \pm 2\%$	$253° \pm 6°$	$17\% \pm 3\%$	$121° \pm 6°$
5°N to 15°N	$11\% \pm 2\%$	$233° \pm 13°$	$29\% \pm 2\%$	$237° \pm 4°$	$16\% \pm 2\%$	$101° \pm 6°$
15°N to 25°N	$19\% \pm 3\%$	$289° \pm 7°$	$16\% \pm 2\%$	$230° \pm 9°$	$9\% \pm 2\%$	$92° \pm 15°$
25°N to 35°N	$7\% \pm 2\%$	$320° \pm 17°$	$7\% \pm 2\%$	$169° \pm 14°$	$7\% \pm 2\%$	$296° \pm 15°$
35°N to 45°N	$4\% \pm 1\%$	$150° \pm 21°$	$8\% \pm 2\%$	$143° \pm 10°$	$8\% \pm 2\%$	$344° \pm 11°$
Tides Identified	SW1		DE1, S0		DE2, SE1	

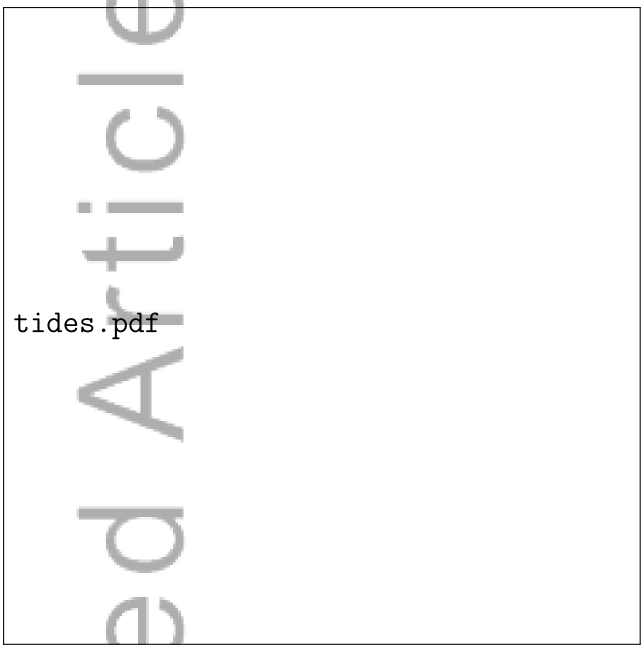

Figure 2. Scaled density at 130 km binned by latitude and longitude, with crosses showing the location of the individual profiles. Observations are made between 1340 − 1500 LST at $L_s = 217^\circ - 219^\circ$. A value of 0.1 ($\mathrm{km}^{-1}$) corresponds to a density of $\sim 10^{11}$ cm^{-3} assuming $\sigma \sim 10^{-17}$ cm^2.

fitplots.pdf

Figure 3. Fit to variations of scaled density at 130 km derived from profiles from $-5°$N to $5°$N (left) and from $35°$N to $45°$N (right). Error bars denote 1σ fit uncertainties. A value of 0.1 (km^{-1}) in scaled density corresponds to a density of $\sim 10^{11}$ cm^{-3} assuming $\sigma \sim 10^{-17}$ cm^2.

fit.pdf

Figure 4. Fitted amplitudes A' and apparent phases δ' for wave-1, wave-2 and wave-3 components for scaled densities at 130 km obtained from profiles grouped by latitude band. Error bars denote 1σ fit uncertainties.

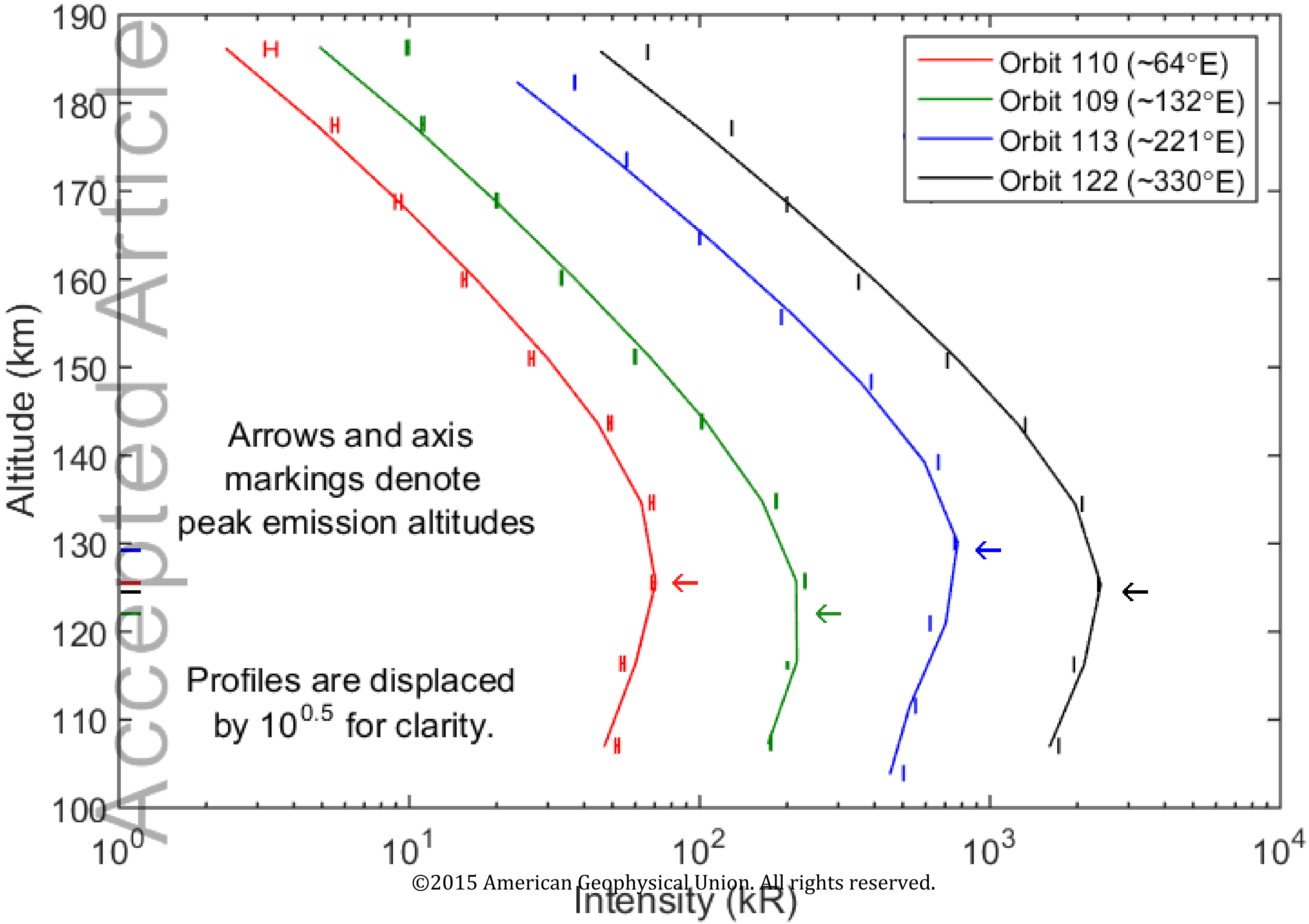

Orbit 110 (~64°E)
Orbit 109 (~132°E)
Orbit 113 (~221°E)
Orbit 122 (~330°E)
Arrows and axis
markings denote
peak emission altitudes
Profiles are displaced
by 10^0.5 for clarity.
Altitude (km)
Intensity (kR)

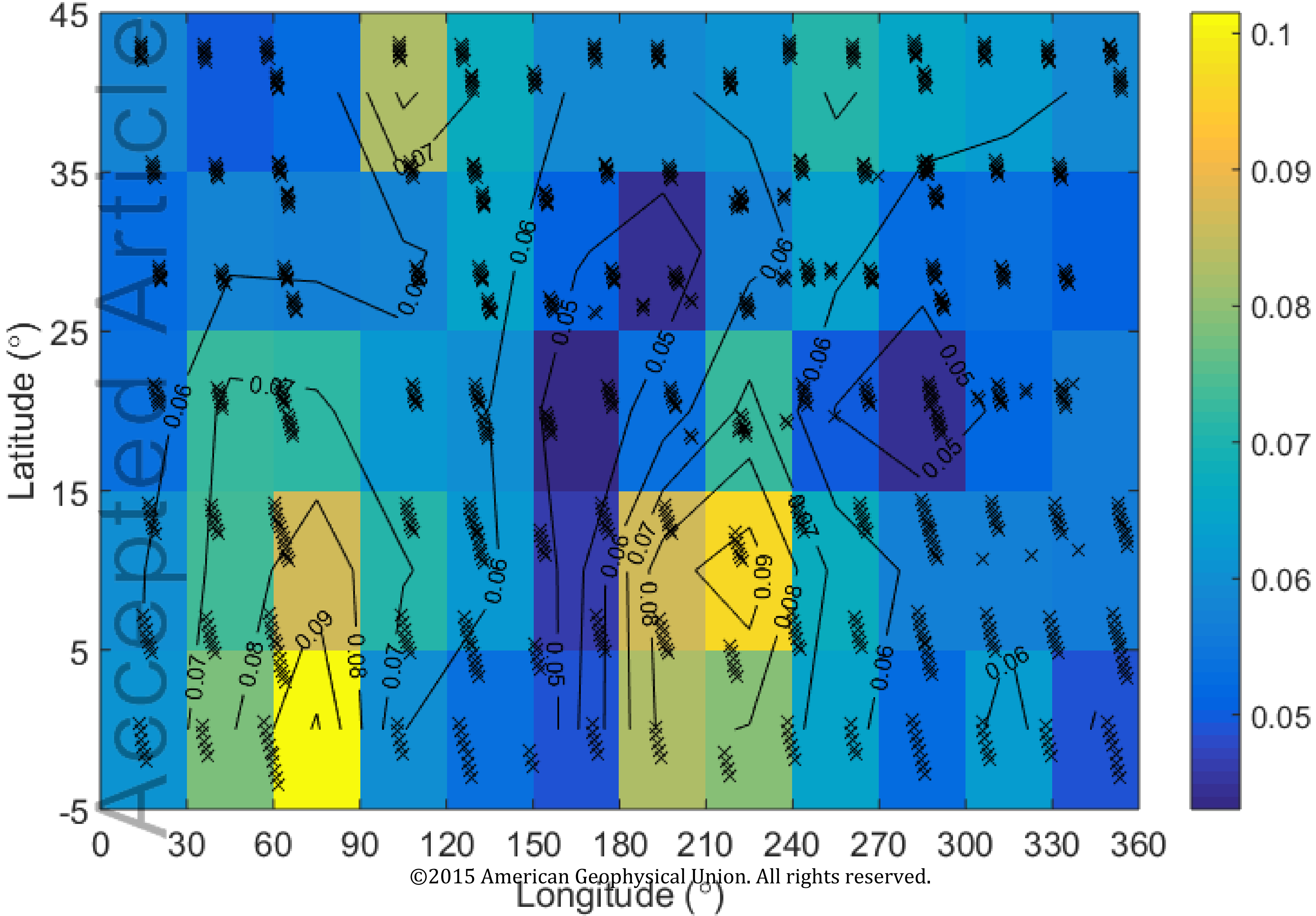
45
35
25
15
5
-5
Latitude (°)
0
30
60
90
120
150
180
210
240
270
300
330
360
Longitude (°)
0.1
0.09
0.08
0.07
0.06
0.05

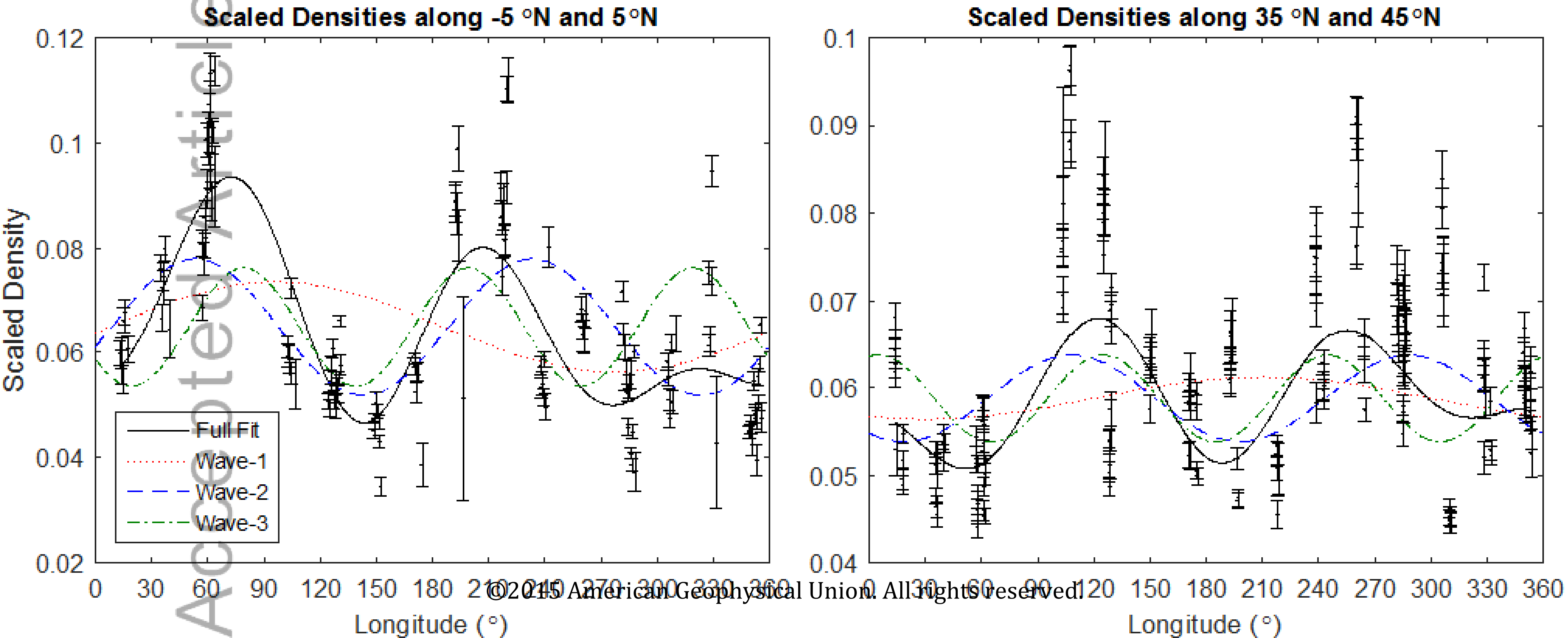
Scaled Densities along -5 °N and 5 °N
Scaled Density
Longitude (°)
Full Fit
Wave-1
Wave-2
Wave-3
0.12
0.1
0.08
0.06
0.04
0.02
0
30
60
90
120
150
180
210
240
270
300
330
360
Scaled Densities along 35 °N and 45 °N
0.1
0.09
0.08
0.07
0.06
0.05
0.04
Longitude (°)

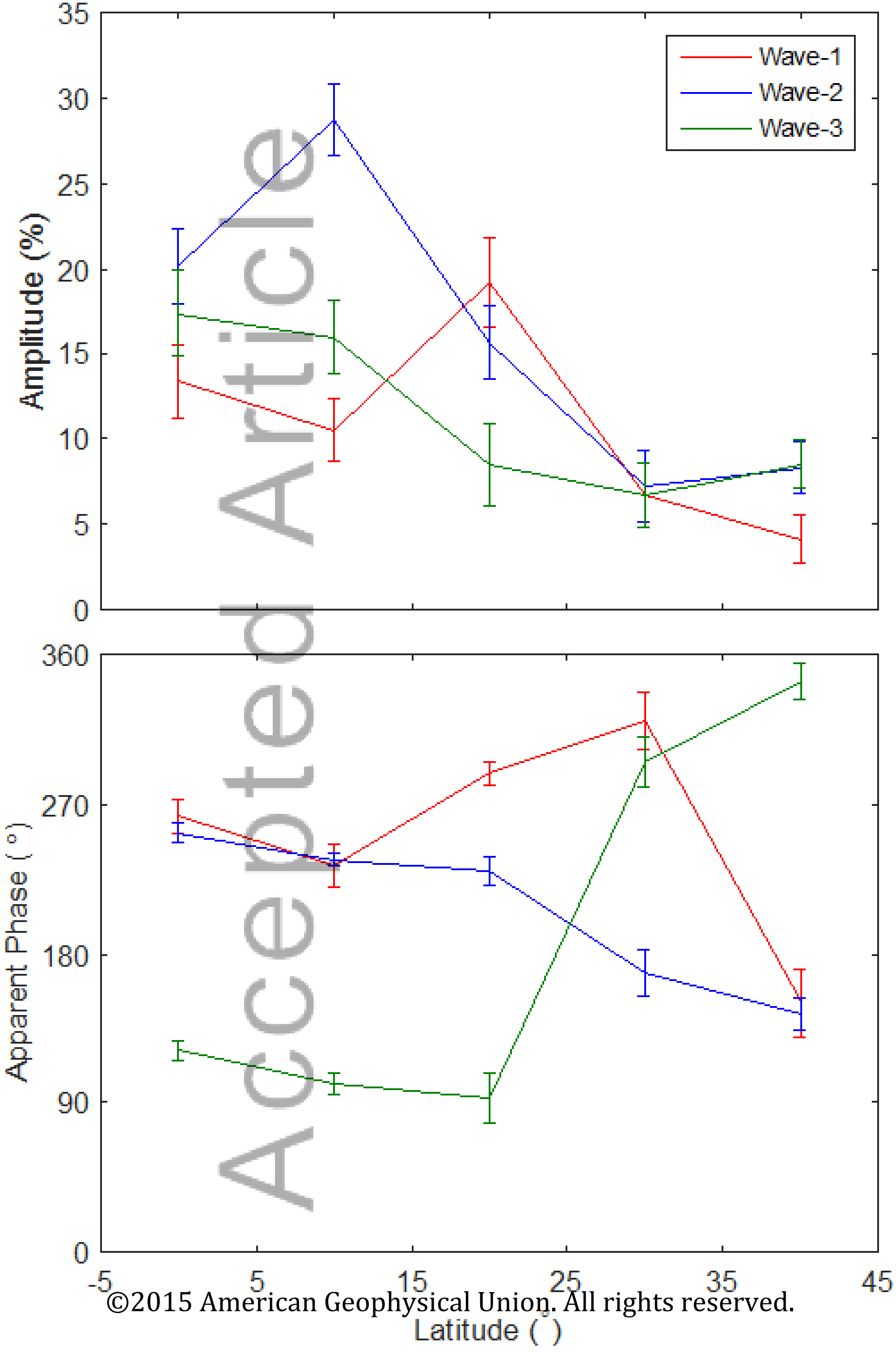
Wave-1
Wave-2
Wave-3
Amplitude (%)
35
30
25
20
15
10
5
0
Apparent Phase (°)
360
270
180
90
0
-5
5
15
25
35
45
Latitude (°)